Chem

CellPress

Article

Dynamic restructuring of epitaxial Au–Cu biphasic interface for tandem CO_2-to-C_{2+} alcohols conversion

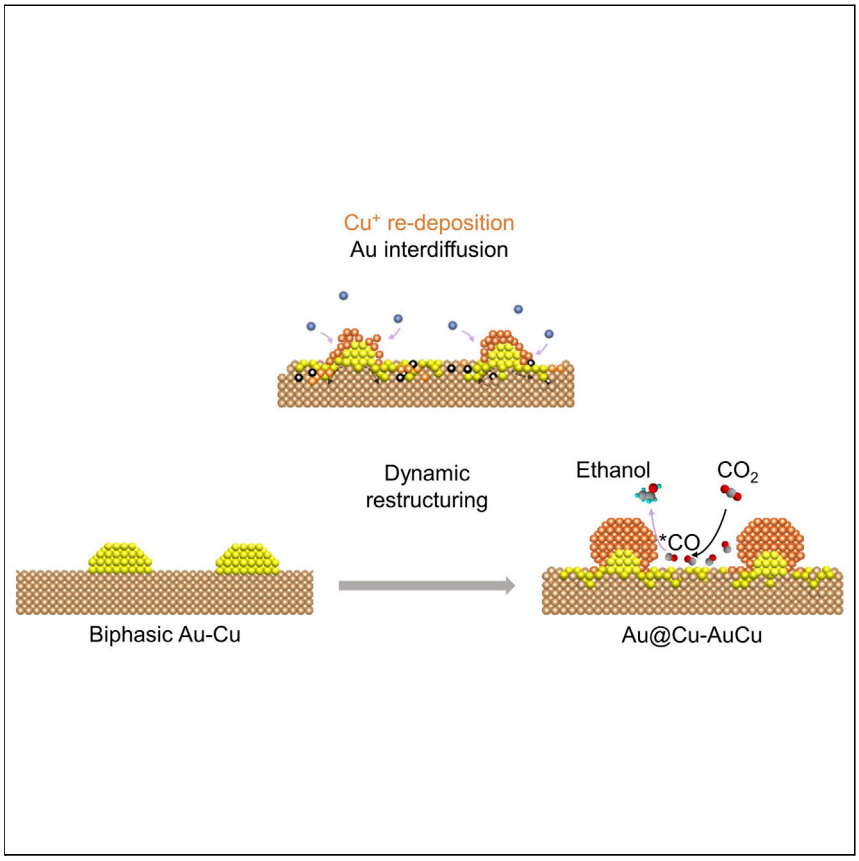

We rationally designed an epitaxial Au–Cu heterostructure as a model system to accurately correlate the atomic reconstruction with catalytic performance and revealed a brand-new insight into tandem CO_2-to-C_{2+} alcohols conversion on bimetallic interface. We illuminated that the *in situ* formed AuCu alloy and Cu shell served as the active phases for *CO buildup and *CO-to-C_{2+} alcohols conversion, respectively, and enriching *CO was a crucial step to keep the durable production of C_{2+} alcohols.

Chenyuan Zhu, Lihui Zhou, Zhibin Zhang, ..., Kaihui Liu, Sheng Dai, Liming Zhang

khliu@pku.edu.cn (K.L.)
shengdai@ecust.edu.cn (S.D.)
zhanglm@fudan.edu.cn (L.Z.)

Highlights

Facet-engineering was adopted to construct an epitaxial Au–Cu biphasic interface

An intermetallic alloying and atomic migration-driven restructuring were revealed

A distinct tandem CO_2-to-C_{2+} alcohols conversion mechanism was proposed

Zhu et al., Chem 8, 1–14
December 8, 2022
https://doi.org/10.1016/j.chempr.2022.08.016

Please cite this article in press as: Zhu et al., Dynamic restructuring of epitaxial Au–Cu biphasic interface for tandem CO_2-to-C_{2+} alcohols conversion, Chem (2022), https://doi.org/10.1016/j.chempr.2022.08.016

Chem

CellPress

Article

Dynamic restructuring of epitaxial Au–Cu biphasic interface for tandem CO_2-to-C_{2+} alcohols conversion

Chenyuan Zhu,[1,4] Lihui Zhou,[2,4] Zhibin Zhang,[3,4] Chunlei Yang,[1] Guoshuai Shi,[1] Siwen Zhao,[1] Huoliang Gu,[1] Jing Wu,[1] Xinyang Gao,[1] Yefei Li,[1] Kaihui Liu,[3,*] Sheng Dai,[2,*] and Liming Zhang[1,5,*]

SUMMARY

Interfacing Cu with a secondary metal is an effective strategy to enhance the production of value-added C_{2+} fuels in CO_2 electroreduction. However, such a biphasic interface generally suffers unclear dynamic reconstruction/phase transformation, rendering the structure-function correlation elusive. Here, we studied a model system of epitaxial Au–Cu heterostructure, which exhibits a ~150 mV more positive onset potential for C_{2+} alcohols and a 400-fold improved alcohols production over hydrocarbons, relative to primitive Cu. We unambiguously revealed a dynamic restructuring of such heterostructure, from phase-separated bimetals to alloy-supported core-shell nanoclusters, driven by the oxidation/reduction of Cu(0) at the interface. A distinct tandem mechanism was proposed, and the buildup of *CO was identified as crucial to keeping the production durability of C_{2+} alcohols. This work fills in the voids of direct observation on the dynamic restructuring of the bimetallic interface and establishes a paradigm to understand the tandem CO_2-to-C_{2+} alcohols conversion from an atomic view.

INTRODUCTION

The over-reliance on fossil fuels gave rise to the global-warming crisis, and thus technologies that are capable of converting greenhouse gas CO_2 to value-added chemicals are therefore of interest.[1,2] Electrochemical CO_2 reduction (CO_2R) holds a great promise to transform CO_2 to valuable fuels and potentially serves as a supplement to the petrochemical feedstock.[3,4] Among various products from CO_2R, multi-carbon (C_{2+}) fuels, such as ethylene, ethanol, and n-propanol, etc., are highly demanded because of their high energy densities and ease of storage/transportation.[5–7] Despite tremendous efforts since the pioneering work of Hori et al.,[8–10] the main hurdle for CO_2R remains the development of highly active, selective, and durable electrocatalysts. Owing to the optimal binding energy with the intermediate *CO, Cu is the only recognized catalyst that can catalyze carbon dimerization and produce value-added C_{2+} fuels.[11–13] However, CO_2R on monometallic Cu is processed at very high overpotentials and, in most cases, suffers from a poor selectivity and yield rate toward C_{2+}, heavily impeding their practical applications.

Interfacing Cu with a secondary metal to form a bimetallic catalyst has been shown effective to enhance the selectivity toward C_{2+} products from tandem electrocatalysis,[14–16] benefiting from the tunable binding energy between the bimetallic catalyst and key intermediates, such as *CO. For instance, Pd–Cu and Ag–Cu bimetallic catalysts have been proven to effectively improve the selectivity toward ethylene,[17–19]

THE BIGGER PICTURE

Electrochemical CO_2 reduction is a promising route to close the anthropogenic carbon cycle and store renewable energy. Interfacing Cu with a secondary metal to form a bimetallic heterostructure has been shown effective to increase the selectivity of C_{2+} fuels via tandem electrocatalysis. However, the lack of atomic-scale structural characterization would impede the fundamental understanding of tandem CO_2-to-C_{2+} conversion. Here, we employed a model system of epitaxial Au–Cu biphasic heterostructure and revealed a dynamic restructuring from phase-separated Au–Cu bimetals to alloy-supported Au@Cu core-shell nanoclusters during electrocatalysis. A distinct tandem mechanism was proposed, and the buildup of *CO was identified as crucial to keeping the production durability of C_{2+} alcohols. This work establishes an empirical demonstration of dynamic reconstruction in a bimetallic model system and sets up a paradigm to understand the tandem CO_2-to-C_{2+} alcohols conversion from an atomic view.

Please cite this article in press as: Zhu et al., Dynamic restructuring of epitaxial Au–Cu biphasic interface for tandem CO_2-to-C_{2+} alcohols conversion, Chem (2022), https://doi.org/10.1016/j.chempr.2022.08.016

and Au–Cu will boost the production of C_{2+} alcohols.[20,21] Most of these studies to date established good understandings toward the improved performances from a theoretical perspective without an in-depth empirical atomic-scale structure characterization. However, the structural dynamics of catalysts in electrocatalysis complicate such theoretical understanding, in particular when phase transformation and surface restructuring occur during CO_2R. The lack of accurate atomic-scale structural characterization would particularly impede the fundamental understanding of tandem CO_2-to-C_{2+} conversion on a bimetallic interface.

Herein, an epitaxial Au–Cu heterostructure was employed as a model system to understand the dynamic reconstruction/phase transformation of the bimetallic interface under CO_2R. Comparing with monometallic Cu, the epitaxial Au–Cu exhibits a ~150 mV more positive onset potential toward C_{2+} alcohols and a 400-fold improvement on the production of alcohols over hydrocarbons at a low overpotential. We probed the bimetallic interface at an atomic scale and observed an unambiguous interface restructuring, from a phase-separated Au–Cu interface to unique AuCu alloy-supported epitaxial Au@Cu core-shell nanoclusters, driven by the oxidation-reduction process of Cu(0) on electrode-electrolyte interface. Combining with *in situ* Fourier-transform infrared (FTIR) spectroscopy, finite-element simulation, and density functional theory (DFT) calculation, we illuminated that the *in situ* formed AuCu alloy and Cu shell serves as the active phase for *CO buildup and *CO-to-C_{2+} alcohols transition, respectively, and enriching *CO is a key step to keep the durable production of C_{2+} alcohols. This work reveals the empirical demonstration to track the atomic restructuring of a model bimetallic system, which not only sets a paradigm to correlate the surface structure and catalytic performance but also brings a brand-new insight to tandem CO_2R on bimetallic electrocatalysts.

RESULTS AND DISCUSSION

Structural characterization of epitaxial Au–Cu heterostructure

A bimetallic interface with a well-defined atomic configuration is fairly important for the subsequent study on dynamic reconstruction. Here, we chose an epitaxial Au–Cu heterostructure as a model system. Typically, Au nanoclusters were electrochemically deposited on a monocrystalline Cu substrate, which was fabricated via our recently developed "seeded growth" technique.[22] The single-crystal nature of Cu support was corroborated by X-ray diffraction (XRD) and selected area electron diffraction (SAED) taken over a large area (Figures S1 and S2). The atomic force microscopy (AFM) and scanning electron microscopy (SEM) images demonstrated an even dispersion of uniform Au nanoclusters after electrodeposition, with a typical size of ~10 nm (Figures 1A and S3). X-ray photoelectron spectroscopy (XPS) measurements showed that the atomic content of Au can be well controlled in the range of 2%–10% depending on the deposition time (Figure S4). As shown in Figure 1B, the Au 4f XPS spectra can be fitted into two symmetric peaks with binding energies of 87.9 ($4f_{5/2}$) and 84.2 ($4f_{7/2}$) eV, respectively, indicative of the existence of Au(0). The Cu $2p_{3/2}$ peak was deconvoluted into three-subpeaks at 932.5, 933.5, and 935.0 eV, respectively, confirming the mixed valence states of Cu(0) and Cu(II). The presence of Cu(II) can be attributed to the formation of an ultrathin CuO and $CuCO_3$ layer after exposing electrode in air.[20,23]

Next, electron microscopy was employed to illuminate the as-prepared Au–Cu interface at an atomic scale. The cross-sectional transmission electron microscopy (TEM) sample was prepared using focused ion beam (FIB), with detailed methods provided in experimental procedures and Figure S5. It was observed that the Cu surface

[1]Department of Chemistry, *i*ChEM (Collaborative Innovation Center of Chemistry for Energy Materials), Shanghai Key Laboratory of Molecular Catalysis and Innovative Materials, Fudan University, Shanghai 200438, China

[2]Key Laboratory for Advanced Materials and Joint International Research Laboratory of Precision Chemistry and Molecular Engineering, Feringa Nobel Prize Scientist Joint Research Center, School of Chemistry and Molecular Engineering, East China University of Science and Technology, Shanghai 200237, China

[3]State Key Laboratory for Mesoscopic Physics, Frontiers Science Center for Nano-optoelectronics, School of Physics, Peking University, Beijing 100871, China

[4]These authors contributed equally

[5]Lead contact

*Correspondence: khliu@pku.edu.cn (K.L.), shengdai@ecust.edu.cn (S.D.), zhanglm@fudan.edu.cn (L.Z.)

https://doi.org/10.1016/j.chempr.2022.08.016

Please cite this article in press as: Zhu et al., Dynamic restructuring of epitaxial Au–Cu biphasic interface for tandem CO_2-to-C_{2+} alcohols conversion, Chem (2022), https://doi.org/10.1016/j.chempr.2022.08.016

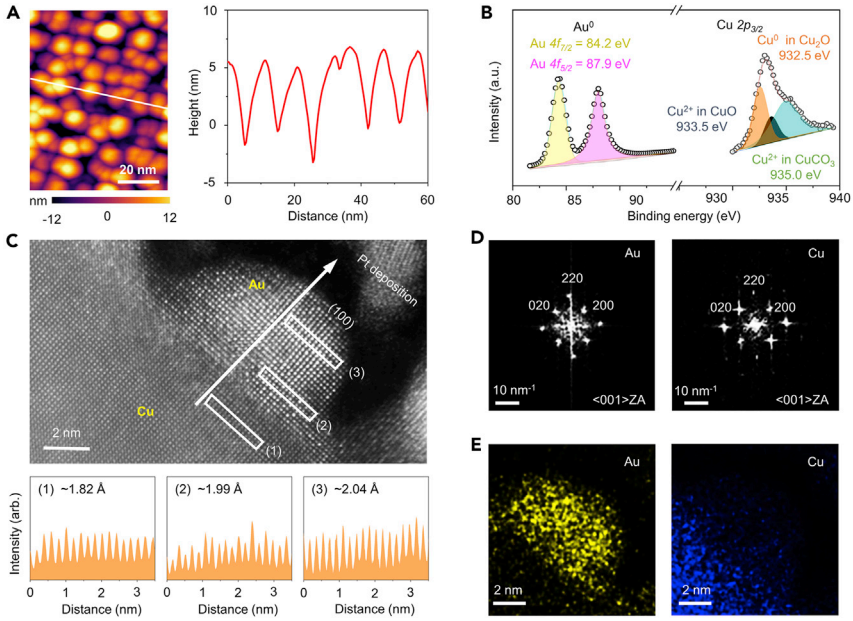

Figure 1. Characterization of the as-prepared epitaxial Au–Cu heterostructure

(A) An AFM image (left) and corresponding height profile (right) along the white line.

(B) Au *4f* and Cu *2p* XPS analysis.

(C) A typical HAADF-STEM image of Au–Cu biphasic interface (top) and intensity line profiles extracted from the solid box (bottom), showing the lattice spacing of {200} increased from 1.82 Å in the bulk of Cu to 1.99 Å at the Au–Cu interface and further increased to 2.04 Å on the top-surface of Au (to protect the Au–Cu interface during the FIB cutting, a thin Pt layer was deposited on top of Au).

(D) FFT patterns taken from Au and Cu regions in (C) at the zone axis of <001>.

(E) EDS elemental maps at Au–Cu interface, showing the separate phases of Au and Cu.

displayed a rough geometry, having series of peaks with vertex angles distributed in the range of 52°–63° (see Figure S2 and Table S1). The scanning TEM (STEM) image illuminated uniform Au clusters coated on the highly uneven Cu surface after electrodeposition (Figure S6). Elaborate TEM imaging and electron diffraction analysis revealed that quantities of Cu peaks exposed (100) terraces (Figures S7 and S8), which is highly likely due to the lowest required formation energy under such Au deposition condition. Furthermore, an epitaxial Au–Cu interface was disclosed by the aberration-corrected high-angle annular dark-field (HAADF)-STEM image based on Z-contrast (Figure 1C). The lattice spacing of {200} increased from 1.82 Å in the bulk of Cu to 1.99 Å at Au–Cu interface and further to 2.04 Å on the top surface of Au where the compressive strain was fully released. Moreover, the fast Fourier transform (FFT) and energy-dispersive X-ray spectroscopy (EDS) analysis verified the separated Au and Cu phases rather than alloyed AuCu (Figures 1D, 1E, and S9). All these characterizations demonstrated the successful preparation of a phase-separated Au–Cu bimetallic heterostructure with a well-defined interfacial atomic configuration.

Electrochemical reduction of CO_2

The CO_2R catalytic activity of Au–Cu heterostructure was examined in CO_2-saturated 0.1 M $KHCO_3$ with a gas-tight H cell. Considering the facet influence, we prepared Cu(100) and Au(100) as control samples, respectively (see details in experimental procedures). To quantitatively determine and compare the catalytic activity, gas products were quantified through the sampling system of an online

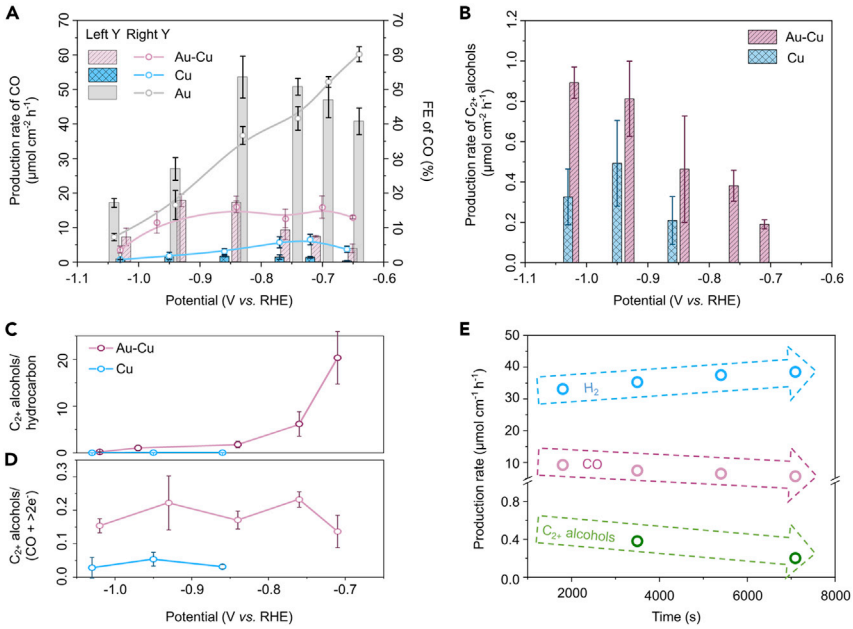

Figure 2. Electrochemical CO_2R measurements

(A) Production rate and FE of CO on Au, Au–Cu, and Cu electrodes.

(B) Production rate of C_{2+} alcohols on Au–Cu and Cu electrodes.

(C and D) Potential dependence of the molar ratio of C_{2+} alcohols to hydrocarbons (C) and alcohols to (CO + >2e$^-$ products) (D) on Au–Cu and Cu.

(E) The stability of production rates of H_2, CO, and C_{2+} alcohols on Au–Cu at −0.75 V versus RHE. All measurements were performed in a CO_2-saturated 0.1 M $KHCO_3$ electrolyte (pH 6.8), and the error bars represent one standard deviation of triplicate measurements.

gas chromatography (GC), whereas the liquid products were collected and analyzed by ^{1}H nuclear magnetic resonance (NMR) spectroscopy. 1 h chronoamperometry (CA) experiments were used to examine the activities of electrocatalyst across a broad range of potentials. The average experimental data, collected for at least three independent samples tested at each potential, were summarized in Figures S10–S12, including J_{total}-V curves, Faradaic efficiencies (FEs), and production rates for each product.

One can see that Cu(100) exhibited a comparable product distribution with that reported in the literature,[24] generating more C_{2+} hydrocarbon products, such as ethylene, than C_{2+} alcohols. In sharp contrast, only hydrogen (H_2), carbon monoxide (CO), and formic acid were detected on Au, in particular, at −0.65 V versus reversible hydrogen electrode (RHE), and CO with a maximum FE of ~60% was the dominant CO_2R product (Figure S11). As shown in Figure 2A, an increasing FE and yield rate of CO on Cu, Au–Cu heterostructure, and Au were observed, consistent with a lower activation energy of Au for CO production, as unveiled by DFT calculations (Figure S13). The distinguished CO production can be also ascribed to the different binding energies between metal and *CO intermediate, e.g., the weak binding energy between Au and *CO promotes CO production,[25] whereas the moderate binding energy between Cu and *CO is beneficial for further *CO reduction and >2e$^-$ fuels (>2 mol of e$^-$ are consumed for the generation of product per mol in CO_2R) production.[14] Au–Cu heterostructure exhibited a fairly modest CO producing capability, with a maximum yield rate of ~18 μmol cm^{-2} h^{-1} at −0.85 V versus RHE, which was ~10-fold higher than Cu, but 3 times inferior to Au.

Please cite this article in press as: Zhu et al., Dynamic restructuring of epitaxial Au–Cu biphasic interface for tandem CO_2-to-C_{2+} alcohols conversion, Chem (2022), https://doi.org/10.1016/j.chempr.2022.08.016

For >2e$^-$ fuels, Au–Cu heterostructure demonstrated a distinct production of C_{2+} alcohols, with a ~150 mV more positive onset potential than Cu and a ~2.5-fold higher CO_2-to-C_{2+} alcohols conversion rate at −1.0 V versus RHE (Figure 2B). We further analyzed the production rates of hydrocarbons (e.g., methane and ethylene) (Figure S12), which followed competing production pathways with C_{2+} alcohols.[26,27] The mole ratio of C_{2+} alcohols/hydrocarbons was used to demonstrate this competition. As shown in Figure 2C, this ratio increased dramatically with an overpotential dropping, indicating C_{2+} alcohols are more preferable at less negative potentials. In particular, Au–Cu heterostructure outperformed Cu to produce alcohols and suppress hydrocarbons, as demonstrated by the positively shifted onset potential of alcohols (−0.7 V versus RHE on Au–Cu and −0.85 V versus RHE on pure Cu), and more importantly, a 400-fold higher ratio of C_{2+} alcohols/hydrocarbons at the onset potential of C_{2+} alcohols. As *CO is regarded as the intermediate for >2e$^-$ products, we next calculated the mole ratio of C_{2+} alcohols/(CO + >2e$^-$ products) to elucidate the electrochemical efficiency of *CO-to-C_{2+} alcohols conversion (Figure 2D). The higher ratio can be clearly identified on Au–Cu heterostructure, which was almost 6-fold higher than that on Cu at −0.85 V versus RHE, further demonstrating a preferred C_{2+} alcohol production. For the durability test, the time-dependent production rate and current density of each product on Au–Cu were plotted in Figures 2E and S14, respectively. It was observed that such Au–Cu heterostructure exhibited a slightly declined CO_2R performance with time, e.g., the yield of CO and C_{2+} alcohols dropped by ~40% (from 9.2 to 5.6 μmol cm^{-2} h^{-1}) and ~49% (from 0.38 to 0.20 μmol cm^{-2} h^{-1}) after 2 h electrocatalysis at −0.75 V versus RHE, respectively. Instead, the production of H_2, as a major competing reaction, increased by ~16%. Such a performance evolution motivated us to probe the structural dynamics on Au–Cu interface down to an atomic scale, in order to elucidate the structure-function correlation.

Atomic reconstruction of Au–Cu interface

Atomic-scale HAADF-STEM imaging was carried out to reveal the Au–Cu interface after 1 h electrocatalysis at −0.75 V versus RHE, and a unique core-shell nanostructure with a typical size of 10–15 nm was observed (Figure 3A). The interplanar d-spacing in the case of the shell can be assigned to Cu(100) planes. As shown in Figure 3B, the lattice fringe spacing of {200} increased from 1.82 Å on the top surface of Cu to 1.85 Å at the nanocluster/substrate interface, highly likely due to the tensile strain because of Au incorporation. Likewise, we characterized the core of this unique structure and identified that Au centered at the core, with a {200} interlayer spacing of 1.96 Å (Figure S15). The valence state of Au remained the same as pristine Au–Cu structure, as demonstrated by XPS analysis (Figure S16). The EDS elemental maps and FFT patterns further verified the location of Au and Cu (Figures 3C, 3D, and S17) and confirmed the Au@Cu core-shell structure. Therefore, the discrete Au nanocluster before CO_2R has been encapsulated in a Cu nanoshell. It is notable that the atomic migration of Cu onto Au was epitaxially, leading to a curved Cu surface together with a nano-space between two neighbored Cu shells.

In addition, the atomic-scale HAADF-STEM image and EDS elemental map at the planar interface corroborated an atomic interdiffusion between Au and Cu atoms (Figures 3E and 3F). The brighter spots showing a higher Z-contrast are corresponding to the Au atoms, proving their diffusion into the Cu matrix. Corresponding FFT patterns at the interface showed superlattice (100) diffraction points (Figure 3G), which is a strong evidence for an intermetallic alloy.[28] Such an evolution happened across the whole surface, and more HAADF-STEM and

Please cite this article in press as: Zhu et al., Dynamic restructuring of epitaxial Au–Cu biphasic interface for tandem CO_2-to-C_{2+} alcohols conversion, Chem (2022), https://doi.org/10.1016/j.chempr.2022.08.016

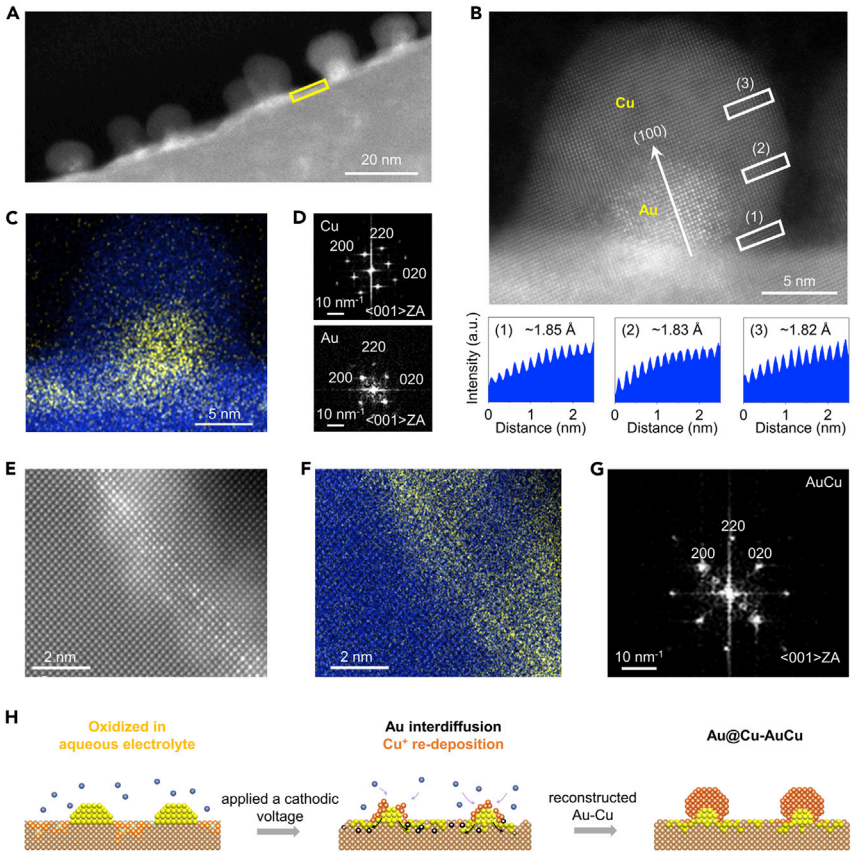

Figure 3. Interface atomic reconstruction

(A) A typical HAADF-STEM image of Au−Cu structure after 1-h CO_2R.

(B) An atomic-scale HAADF-STEM image of Au@Cu core-shell clusters after reconstruction and corresponding intensity line profiles extracted from the white solid boxes.

(C) Corresponding EDS elemental maps of Au@Cu core-shell clusters.

(D) FFT patterns of Cu shell and Au core at the zone axis of <001>, respectively.

(E and F) (E) Representative atomic-scale HAADF-STEM image and (F) EDS elemental map from interfacial region (yellow rectangle in [A]) after reconstruction.

(G) Corresponding FFT pattern of (E) showing the formation of intermetallic alloy.

(H) Proposed structural reconstruction and phase transformation of Au–Cu during CO_2R (golden: Au, coppery: Cu, orange: oxidized Cu, green: O, black: atomic vacancies, bronze: re-deposited Cu, and dark blue: Cu ions).

EDS results on other positions can be found in Figures S17 and S18. This unique finding validates the statement that Au–Cu biphasic interface undergoes a severe reconstruction during CO_2R, leading to a structural transformation from phase-separated bimetals to AuCu alloy-supported epitaxial Au@Cu core-shell nanoclusters.

The dynamic restructuring of Au–Cu interface can be ascribed to the oxidation/reduction of Cu(0) during electrocatalysis, as illustrated by the schematic illustration shown in Figure 3H. At an open circuit potential, the Cu(0) exposed to electrolyte without Au protection is prone to be oxidized to Cu(I) and Cu(II),[29,30] and such chemical oxidation damages the well-defined atomic structure because of oxygen incorporation. Some Cu atoms are even released to electrolyte and generate a certain concentration of Cu ions, as verified by the inductively coupled plasma optical

Please cite this article in press as: Zhu et al., Dynamic restructuring of epitaxial Au–Cu biphasic interface for tandem CO_2-to-C_{2+} alcohols conversion, Chem (2022), https://doi.org/10.1016/j.chempr.2022.08.016

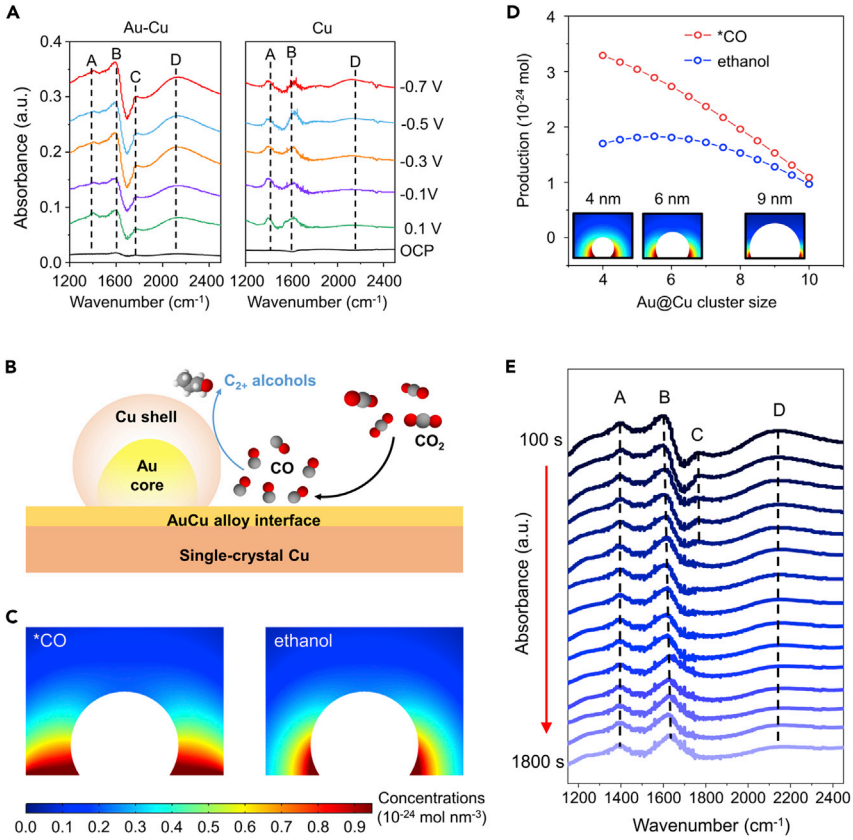

Figure 4. Mechanistic understanding

(A) *In-situ* FTIR spectra of Au–Cu (left) and Cu (right) electrodes during the cathodic scan (V versus RHE) in a CO_2-saturated 0.1 M $KHCO_3$ solution.

(B) The schematic diagram of "tandem" electrocatalysis pathway on reconstructed Au–Cu electrode.

(C) An overview of the concentration and flux distribution of *CO and ethanol on a reconstructed Au-Cu heterostructure with 5.5 nm radius of Cu shell at −0.75 V *vs.* RHE.

(D) The production of *CO and ethanol as a function of the size of Au@Cu cluster.

(E) Time-dependent electrochemical *in-situ* FTIR spectra of Au–Cu electrode at −0.75 V versus RHE.

emission spectrometry (ICP-OES) (Table S2). Under a cathodic bias, the oxygen removal will lead to the reduction of Cu(I) and Cu(II) and spontaneously leave abundant of atomic vacancies,[31] which will greatly facilitate the atomic interdiffusion between Au and Cu, leading to AuCu alloy after applying a cathodic potential. At the same time, the electrochemical reduction will result in a redeposition of Cu ions from electrolyte, and such redeposition is prone to occur locally on the top surface of Au nanoclusters owing to their lower adsorption energies, followed by the formation of epitaxially Au@Cu core-shell nanoclusters. As far as we know, this is the first time to report the dynamic restructuring of Cu-based bimetallic heterostructure down to an atomic scale during tandem CO_2R electrocatalysis.

Structure-property correlation

We employed *operando* FTIR spectroscopy to probe the adsorbate intermediates on both Au–Cu and Cu at different potentials. Four major peaks were explicitly discerned on Au–Cu surface (Figure 4A). The peak A appearing at 1,393–1,401 cm^{-1} was attributed to CO_3^{2-}, whereas peak B at 1,620 cm^{-1} was assigned to the H–O–H bending mode of H_2O ($\delta_{(H-O-H)}$).[32,33] The band at 1,760 cm^{-1}, peak C,

Please cite this article in press as: Zhu et al., Dynamic restructuring of epitaxial Au–Cu biphasic interface for tandem CO_2-to-C_{2+} alcohols conversion, Chem (2022), https://doi.org/10.1016/j.chempr.2022.08.016

was in close proximity to the stretching of *CHO, which served as an important precursor for the subsequent C–C coupling.[34] The band at ~2,100 cm^{-1} (peak D), intensifying at more negative potentials, was attributed to the C≡O stretching mode of atop-bonded *CO adlayers.[35] In contrast to Au–Cu, Cu surface exhibited two strong bands assignable to CO_3^{2-} and H_2O at 1,393–1,401 cm^{-1} (peak A) and 1,620 cm^{-1} (peak B), respectively. The peak D for *CO adsorbates at ~2,100 cm^{-1} was much more inexplicit across the potential window. The negative band at ~2,345 cm^{-1} on Cu was assigned to CO_2 molecules in aqueous electrolyte.[32] These spectroscopic results demonstrated that Au–Cu electrode exhibited a higher coverage of *CO, a critical intermediate in the producing pathway of C_{2+} alcohols. The enriched *CO provided a microenvironment that can lower down the reaction barrier for C–C coupling and steered the selectivity toward C_{2+} alcohols at a lower overpotential.[36] Moreover, such *in situ* produced *CO cannot be replaced by CO supplying reagent, as the production rates of alcohols from the direct CO reduction on Cu and Au–Cu were both orders of magnitudes lower than that from CO_2R (Figure S19). Furthermore, Cu–Au exhibited scarcely any production preference toward C_{2+} alcohols comparing with pure Cu. These observations experimentally proved the importance of locally enriched *CO for tandem catalysis on reconstructed Au–Cu surface.

The conventional view on tandem catalysis stated that CO_2 would be first reduced to *CO on the secondary metal, such as Zn,[16] Pd,[17] Ag,[18,19] and Au,[20] etc., building up a super-high *CO concentration in the vicinity, which would undergo dimerization and further be reduced to a higher-valued product on Cu. By contrast, our results proved that the biphasic interface will experience a significant dynamic reconstruction under CO_2R, which leads to evolution of active phases, suggesting that the classic tandem picture of electrocatalysis on biphasic interface may be insufficient. From our observations, the Au nanoclusters were fully encapsulated in a Cu shell and could not serve as efficient CO producing sites. Instead, the *in situ* generated AuCu alloy served as the active phase to buildup *CO at the interface, as inspired from Kim et al.[37] Following, the *in situ* formed Cu shell would convert *CO to C_{2+} alcohols. This mechanism was schematically shown in Figure 4B. Such a tandem picture can be also visualized via finite-element simulation (see details in experimental procedures). We set up a full micro-kinetic model that took into account all key elementary steps from CO_2 to ethanol, including CO_2-to-*CO conversion on AuCu alloy support and Cu shell as well as *CO-to-ethanol conversion on Cu shell. As demonstrated in Figure 4C, *CO mainly generated on AuCu alloy surface and quickly diffused to the electrolyte (as CO molecules). Instead, ethanol preferred to generate at the Cu shell neighboring the AuCu alloy, where *CO was mostly enriched, unveiling a synergistic interaction of two phases for the tandem CO_2-to-alcohols production.

We attempted to correlate the yields of *CO and ethanol with the size of reconstructed Au@Cu clusters (Figures S20 and S21). Notably, the size increasing of Au@Cu cluster will lead to a higher coverage of Cu shell, whereas a lower coverage of exposed planar AuCu alloy. Figure 4D evidenced that at a given potential, both *CO and ethanol exhibited size-dependent production rates. The generation of *CO strongly declined with the increasing size of Cu shell, which could be attributed to the drop of AuCu area exposed. In stark contrast, the production of ethanol first showed a weakly positive correlation with Au@Cu cluster size below 5.5 nm, which, however, turned to a modestly negative correlation as the size increasing, suggesting the optimal size of Cu shell would be 5.5 nm. It is worth noting that the yields of *CO and ethanol showed a similar correlation when the size was higher than 9 nm,

indicating that although a larger curving Cu shell provided more active sites for *CO-to-C_{2+} alcohols conversion, the buildup of *CO determined the production rates of C_{2+} alcohols.

To unveil the influence of surface reconstruction on *CO enrichment, time-dependent *in situ* FTIR and DFT calculation were further performed. The FTIR spectra in Figure 4E showed that the intensity of *CHO and atop-bonded *CO (peak C and D, at 1,760 cm^{-1} and ~2,100 cm^{-1}, respectively) gradually weakened with time prolonged, suggesting the reconstruction was detrimental to buildup *CO intermediate. DFT calculation was explored to reveal how the *CO coverage influenced C_{2+} alcohols generation on Cu surface (see supplemental information for details). We calculated the energy diagrams associated with hydrogenation along the formation pathway of ethanol at different *CO coverages. Results demonstrated that the energy barrier required for *HCCOH-to-*HCCHOH (rate-determining step)[38,39] increased at a lower *CO coverage (Figure S22). Therefore, it is reasonable to ascribe the gradually dropped yield of C_{2+} alcohols to the limited source of *CO intermediate from surface reconstruction. These observations were consistent with the declined yields of CO and C_{2+} alcohols with time shown in Figure 2E.

Conclusions

In summary, we studied a model system of epitaxial Au–Cu heterostructure having a biphasic interface for CO_2R, which demonstrated a remarkable tandem CO_2-to-C_{2+} alcohols conversion. Utilizing aberration-corrected HAADF-STEM, a dynamic structural reconstruction/transformation from bimetallic separated-phase into alloy-supported core-shell nanoclusters was evidently unveiled during the reaction. We proposed a novel CO_2-to-C_{2+} alcohols conversion mechanism distinguished with the conventional view and correlated the evolution of CO_2R performance to the limited supply of *CO intermediates. This work establishes the empirical demonstration of dynamic structural reconstruction/transformation in the bimetallic model system and sets up a paradigm to understand the tandem CO_2-to-C_{2+} alcohols conversion from an atomic view.

EXPERIMENTAL PROCEDURES

Resource availability

Lead contact

Further information and requests for resources and reagents should be directed to the lead contact, Liming Zhang (zhanglm@fudan.edu.cn).

Materials availability

The materials generated in this study will be made available on request.

Data and code availability

All of the data are available from the corresponding author upon reasonable request.

Synthesis of epitaxial Au–Cu bimetallic heterostructure

The single-crystal Cu substrate was prepared via the "seeded abnormal grain growth" strategy following our previous report.[22] Prior to deposit Au, the single-crystal Cu substrate was first smoothed by electrochemical polishing in an electrolyte composed of H_3PO_4 and H_2SO_4 with a voltage of 2 V for 2 s. After cleaning, the single-crystal Cu substrate was immediately moved to an electrolyte consisting of 0.05 mM $HAuCl_4$, 0.1 mM KCl, 0.1 mM K_2SO_4, and 1 mM H_2SO_4. The Au

Please cite this article in press as: Zhu et al., Dynamic restructuring of epitaxial Au–Cu biphasic interface for tandem CO_2-to-C_{2+} alcohols conversion, Chem (2022), https://doi.org/10.1016/j.chempr.2022.08.016

nanoclusters were epitaxially grown on Cu via electrochemical deposition at −0.3 V versus Ag/AgCl for 30 s. After that, the Au–Cu heterostructure was cleaned by 0.1 M $HClO_4$ and milli-Q water to remove the residual acid.

TEM samples preparation and characterization

Cross-section TEM samples were prepared using FIB on a Thermofisher Helios G4 dual-beam system. Figure S5 schematically showed the procedure to prepare TEM samples by FIB. Pt was deposited on catalyst as a protection layer prior to the ion beam cutting. Typically, a thin Pt layer of 0.5 μm was first deposited using a mild electron beam (2 kV, 0.2 nA), which could eliminate any possible damages on the catalyst surface. Afterward, ion beam deposition (30 kV, 0.43 nA) was applied to deposit a thick Pt layer of 2.0 μm at the same region. Any possible damages from the ion beam deposition could be alleviated because the catalyst surface was already covered by Pt. To this end, the surface configuration of catalyst could be well preserved. Aberration-corrected STEM characterization was performed on a Thermosisher Themis Z microscope equipped with two aberration correctors under 300 kV. HAADF-STEM images were recorded using a convergence semi angle of 11 mrad, and inner and outer collection angles of 59 and 200 mrad, respectively. EDS was carried out using 4 in-column Super-X detectors.

Other physical characterizations

The XRD of the Cu foils was characterized by Bruker D2 PHASER. XPS (PHI 5000) measurements were carried out using a Mg Kα source, with the pressure inside the chamber maintained below 4×10^{-9} Torr and spectra were collected at a pass energy of 17.9 eV. The highest peak in C 1s spectra was shifted to 284.8 eV for charge correction. AFM (Cypher ES, AR) in tapping mode was used for geometry and morphology studies. Raman spectra were taken by a Horiba HR800 system with a laser excitation energy of 638 nm. The laser spot size was 1 μm and a laser power of 5 mW was used to avoid heating.

Electrochemical CO_2R measurement

The electrocatalytic characterization was carried out in a customized H cell, which has two compartments separated by an anion exchange membrane (Fumatech company, Fumasep FAA-3-PK130). Each compartment contains 6 mL of 0.1 M $KHCO_3$ aqueous solution (pH 6.8) and the compartment holding the working electrode is sealed to measure gaseous products. The electrolyte was purged with CO_2 at a constant flow rate of 20 sccm for 20 min before and during each measurement while stirring. A platinum wire and a Ag/AgCl (CHI, 3 M KCl) were used as counter and reference electrodes, respectively. The potentials measured were converted to RHE scale by V (versus RHE) = V (versus Ag/AgCl, 3 M KCl) + 0.210 V + 0.0591 × pH. The solution resistance was compensated for 85% by the potentiostat and the rest 15% was post-corrected.

All electrochemical measurements were explored using a Biologic-SP300 potentiostat. Before electrolysis, linear sweep voltammetry (at a scan rate of 20 mV s^{-1}) was performed and then a set potential was applied for CA. During the 1-h constant potential electrolysis, the gaseous products were quantified using a GC (Agilent 7890B; column HP-PLOT and MS-5A). Sample for GC was collected at 20-min intervals and the separated gaseous products were analyzed by both thermal conductivity detector (for H_2) and flame ionization detector (for CO, methane, and ethylene). Liquid

products were analyzed afterward by 500 MHz NMR (AVANCE III HD) using dimethyl sulfoxide and phenol as internal standards. Solvent pre-saturation technique was implemented to suppress the water peak.

The FE and production rate can be calculated as follows:

Calculation of the FE of gas products:

$$FE(gas) = \frac{F_{flow} \times (C_{gas}/V_m) \times n \times F}{I_{total} \times 60} \times 100$$

Calculation of the FE of liqiud products:

$$FE(liquid) = \frac{C_{liquid} \times V \times n \times F}{Q_{total}} \times 100$$

Calculation of the production rate of products:

$$Production\ Rate = \frac{FE_{prducts} \times I_{total}}{n \times F} \times 3,600 \times 1,000$$

FE (gas): FE of gas product, %
FE (liquid): FE of liquid product, %
F_{flow}: flow rate of CO_2, mL min^{-1}
C_{gas}: volume ratio of gas product, determined by on-line GC
V_m: the molar volume of an ideal gas at 1 atmosphere of pressure (molar volume at normal temperature and pressure is 0.0245 mL), mL mol^{-1}
C_{liquid}: concentration of liquid product after 1 h of electrolysis, determined by NMR, mol L^{-1}
V: volume of the electrolyte in the working cell, L
I_{total}: steady-state cell current
Q_{total}: total charge in 1 h of bulk electrolysis, C
n: number of transferred electrons for certain product
F: Faradaic constant, 96,485 C mol^{-1}

DFT calculation

All the calculations were performed using DFT as implemented in the Vienna *ab initio* simulation package (VASP). The ion-electron interactions were treated with the projected augmented wave (PAW) pseudopotentials, and the plane-wave basis set was cut off at 400 eV. The general gradient approximation (GGA) parameterized by Perdew, Burke, and Ernzerhof (PBE) was adopted to describe the exchange-correlation functional in structural relaxations. All structures were fully relaxed by a conjugate gradient method until the residual force component was less than 0.08 eV/Å. The centered (4 × 4 × 1) k-point grids were used. The constrained Broyden dimer method was used to locate the transition state. The solvent effect was simulated by using the continuum solvation model based on Poisson-Boltzmann equation, as implemented in the VASPsol code. The pressure of CO is set as 1 atm, the electrode potential U at −0.5 V versus RHE. The computational hydrogen electrode (CHE) is utilized to determine the coverage of H atoms at this electrode potential. The Cu (110) facet is covered by 1 ML *H, whereas the Au (110) face are covered by 0.5 ML *H, respectively. The Gibbs free energies (ΔG) of different intermediates were calculated to characterize the CO_2R performance on Cu facets.

Finite-element simulation

Finite-element simulations were performed using the COMSOL Multiphysics software package. Three modules were used to establish a comprehensive chemistry-mass transport model of the Au–Cu heterostructure. First, the "Chemistry" module was used to define the tandem CO_2R steps. The formation of key CO intermediate from CO_2 on Cu and Au surface were both calculated, defined as the feedstock to ethanol generated from Cu substrate. Second, the "Transport of Diluted Species" module was used to solve the mass transport of three species. We determined the diffusion coefficients and rate constants of chemical reactions by sweeping these parameters over a large range (2 orders of magnitude) and fitting to those electrochemical CO_2R data. There were six parameters that we swept: three diffusion coefficients, D_{eq} CO_2, D_{eq} CO, and D_{eq} ethanol, as well as the rate constants, K_{f1} and K_{f2} of the CO_2 to CO on AuCu and Cu shell, and K_{f3} of the CO-to-ethanol steps.

In situ spectroelectrochemical experiments

In situ FTIR experiments were carried out on a Nicolet 6700 spectrometer with an external mode, equipped with a mercury cadmium telluride detector and p-polarized light. The customized spectroelectrochemical cell was integrated with a prismatic CaF_2 window. The cell was filled with CO_2-satuareted 0.1 M $KHCO_3$ electrolyte. In the thin layer configuration, each spectrum represented the average of 64 interferograms with a resolution of 4 cm^{-1}. The spectra presented with positive bands corresponded to the formation of species, whereas negative bands indicated the consumption of species. All *in situ* FTIR experiments were performed at an ambient environment, and Ag/AgCl and carbon rod were engaged as the reference and counter electrodes, respectively.

SUPPLEMENTAL INFORMATION

Supplemental information can be found online at https://doi.org/10.1016/j.chempr.2022.08.016.

ACKNOWLEDGMENTS

This research was supported by the National Natural Science Foundation of China (grants 21872039, 22072030, 51991340, 51991342, and 52025023), the Fundamental Research Funds for the Central Universities (20720220008 and JKVJ1221022), the Science and Technology Commission of Shanghai Municipality (grants 18JC1411700 and 19DZ2270100), the Beijing Natural Science Foundation (JQ19004), the Shanghai Rising-star Program (20QA1402400), the Program for Professor of Special Appointment (Eastern Scholar) at Shanghai Institutions of Higher Learning, and The Key R&D Program of Guangdong Province (2020B010189001, 2018B030327001). C.Z. thanks the funding support from the China Postdoctoral Science Foundation (2021M700810). Additional support was provided by the Frontiers Science Center for Materiobiology and Dynamic Chemistry and the Feringa Nobel Prize Scientist Joint Research Center at the East China University of Science and Technology.

AUTHOR CONTRIBUTIONS

L.Zhang designed and conceived the experiment. C.Z., S.Z., G.S., H.G., J.W., and X.G. fabricated the electrodes and performed the electrochemical characterization and data analysis. Z.Z. and K.L. carried out the synthesis of single-crystal Cu foils. L.Zhou and S.D. carried out the TEM characterization. Y.L. worked on the DFT calculations. C.Y. helped on the FEM modeling and data fitting. C.Z., S.D., and L.Zhang wrote the manuscript. All authors discussed the results and commented on the paper.

DECLARATION OF INTERESTS

The authors declare no competing interests.

Received: March 27, 2022
Revised: July 6, 2022
Accepted: August 20, 2022
Published: September 14, 2022

REFERENCES

1. Appel, A.M., Bercaw, J.E., Bocarsly, A.B., Dobbek, H., DuBois, D.L., Dupuis, M., Ferry, J.G., Fujita, E., Hille, R., Kenis, P.J.A., et al. (2013). Frontiers, opportunities, and challenges in biochemical and chemical catalysis of CO_2 fixation. Chem. Rev. *113*, 6621–6658.

2. Montoya, J.H., Seitz, L.C., Chakthranont, P., Vojvodic, A., Jaramillo, T.F., and Nørskov, J.K. (2016). Materials for solar fuels and chemicals. Nat. Mater. *16*, 70–81.

3. Kondratenko, E.V., Mul, G., Baltrusaitis, J., Larrazabal, G.O., and Perez-Ramírez, J. (2013). Status and perspectives Co2 conversion into fuels and chemicals by catalytic, photocatalytic and electrocatalytic processes. Energy Environ. Sci. *6*, 3112–3135.

4. Ross, M.B., De Luna, P.D., Li, Y., Dinh, C.T., Kim, D., Yang, P., and Sargent, E.H. (2019). Designing materials for electrochemical carbon dioxide recycling. Nat. Catal. *2*, 648–658.

5. Arán-Ais, R.M., Gao, D., and Roldan Cuenya, B.R. (2018). Structure- and electrolyte-sensitivity in CO_2 electroreduction. Acc. Chem. Res. *51*, 2906–2917.

6. Nitopi, S., Bertheussen, E., Scott, S.B., Liu, X., Engstfeld, A.K., Horch, S., Seger, B., Stephens, I.E.L., Chan, K., Hahn, C., et al. (2019). Progress and perspectives of electrochemical CO_2 reduction on copper in aqueous electrolyte. Chem. Rev. *119*, 7610–7672.

7. Birdja, Y.Y., Pérez-Gallent, E., Figueiredo, M.C., Göttle, A.J., Calle-Vallejo, F., and Koper, M.T.M. (2019). Advances and challenges in understanding the electrocatalytic conversion of carbon dioxide to fuels. Nat. Energy *4*, 732–745.

8. Hori, Y., Kikuchi, K., and Suzuki, S. (1985). Production of CO and CH_4 in electrochemical reduction of CO_2 at metal electrodes in aqueous hydrocarbonate solution. Chem. Lett. *14*, 1695–1698.

9. Hori, Y., Wakebe, H., Tsukamoto, T., and Koga, O. (1994). Electrocatalytic process of CO selectivity in electrochemical reduction of CO_2 at metal electrodes in aqueous media. Electrochim. Acta *39*, 1833–1839.

10. Gao, D., Arán-Ais, R.M., Jeon, H.S., and Roldan Cuenya, B.R. (2019). Rational catalyst and electrolyte design for CO_2 electroreduction towards multicarbon products. Nat. Catal. *2*, 198–210.

11. Kuhl, K.P., Cave, E.R., Abram, D.N., and Jaramillo, T.F. (2012). New insights into the electrochemical reduction of carbon dioxide on metallic copper surfaces. Energy Environ. Sci. *5*, 7050–7059.

12. Peterson, A.A., Abild-Pedersen, F., Studt, F., Rossmeisl, J., and Nørskov, J.K. (2010). How copper catalyzes the electroreduction of carbon dioxide into hydrocarbon fuels. Energy Environ. Sci. *3*, 1311–1315.

13. Zhu, C., Zhang, Z., Zhong, L., Hsu, C.S., Xu, X., Li, Y., Zhao, S., Chen, S., Yu, J., Chen, S., et al. (2021). Product-specific active site motifs of Cu for electrochemical CO_2 reduction. Chem *7*, 406–420.

14. Vasileff, A., Xu, C., Jiao, Y., Zheng, Y., and Qiao, S.Z. (2018). Surface and interface engineering in copper-based bimetallic materials for selective CO_2 electroreduction. Chem *4*, 1–2.

15. Zhu, C., Zhao, S., Shi, G., and Zhang, L. (2021). Structure-function correlation and dynamic restructuring of Cu for highly efficient electrochemical CO_2 conversion. ChemSusChem *15*, e202200068.

16. Ren, D., Ang, B.S.H., and Yeo, B.S. (2016). Tuning the selectivity of carbon dioxide electroreduction toward ethanol on oxide-derived Cu_xZn catalysts. ACS Catal *6*, 8239–8247.

17. Ma, S., Sadakiyo, M., Heima, M., Luo, R., Haasch, R.T., Gold, J.I., Yamauchi, M., and Kenis, P.J.A. (2017). Electroreduction of carbon dioxide to hydrocarbons using bimetallic Cu-Pd catalysts with different mixing patterns. J. Am. Chem. Soc. *139*, 47–50.

18. Huang, J., Mensi, M., Oveisi, E., Mantella, V., and Buonsanti, R. (2019). Structural sensitivities in bimetallic catalysts for electrochemical CO_2 reduction revealed by Ag-Cu nanodimers. J. Am. Chem. Soc. *141*, 2490–2499.

19. Chen, C., Li, Y., Yu, S., Louisia, S., Jin, J., Li, M., Ross, M.B., and Yang, P. (2020). Cu–Ag tandem catalysts for high-rate CO_2 electrolysis toward multicarbons. Joule *4*, 1688–1699.

20. Morales-Guio, C.G., Cave, E.R., Nitopi, S.A., Feaster, J.T., Wang, L., Kuhl, K.P., Jackson, A., Johnson, N.C., Abram, D.N., Hatsukade, T., et al. (2018). Improved CO_2 reduction activity towards C_{2+} alcohols on a tandem gold on copper electrocatalyst. Nat. Catal. *1*, 764–771.

21. Lum, Y., and Ager, J.W. (2018). Sequential catalysis controls selectivity in electrochemical CO_2 reduction on Cu. Energy Environ. Sci. *11*, 2935–2944.

22. Wu, M., Zhang, Z., Xu, X., Zhang, Z., Duan, Y., Dong, J., Qiao, R., You, S., Wang, L., Qi, J., et al. (2020). Seeded growth of large single-crystal copper foils with high-index facets. Nature *581*, 406–410.

23. Kim, J., Choi, W., Park, J.W., Kim, C., Kim, M., and Song, H. (2019). Branched copper oxide nanoparticles induce highly selective ethylene production by electrochemical carbon dioxide reduction. J. Am. Chem. Soc. *141*, 6986–6994.

24. Huang, Y., Handoko, A.D., Hirunsit, P., and Yeo, B.S. (2017). Electrochemical reduction of CO_2 using copper single-crystal surfaces: effects of *CO coverage on the selective formation of ethylene. ACS Catal *7*, 1749–1756.

25. Back, S., Yeom, M.S., and Jung, Y. (2015). Active sites of Au and Ag nanoparticle catalysts for CO_2 electroreduction to CO. ACS Catal *5*, 5089–5096.

26. Li, Y.C., Wang, Z., Yuan, T., Nam, D.H., Luo, M., Wicks, J., Chen, B., Li, J., Li, F., de Arquer, F.P.G., et al. (2019). Binding site diversity promotes CO_2 electroreduction to ethanol. J. Am. Chem. Soc. *141*, 8584–8591.

27. Karapinar, D., Creissen, C.E., Rivera de la Cruz, J.G., Schreiber, M.W., and Fontecave, M. (2021). Electrochemical CO_2 reduction to ethanol with copper-based catalysts. ACS Energy Lett *6*, 694–706.

28. He, R., Wang, Y.C., Wang, X., Wang, Z., Liu, G., Zhou, W., Wen, L., Li, Q., Wang, X., Chen, X., et al. (2014). Facile synthesis of pentacle gold-copper alloy nanocrystals and their plasmonic and catalytic properties. Nat. Commun. *5*, 4327.

29. Ren, D., Deng, Y., Handoko, A.D., Chen, C.S., Malkhandi, S., and Yeo, B.S. (2015). Selective electrochemical reduction of carbon dioxide to ethylene and ethanol on copper(i) oxide catalysts. ACS Catal *5*, 2814–2821.

30. Lee, S.H., Lin, J.C., Farmand, M., Landers, A.T., Feaster, J.T., Avilés Acosta, J.E., Beeman, J.W., Ye, Y., Yano, J., Mehta, A., et al. (2021). Oxidation state and surface reconstruction of Cu under CO_2 reduction conditions from *in situ* X-ray characterization. J. Am. Chem. Soc. *143*, 588–592.

31. Chang, C.J., Lin, S.C., Chen, H.C., Wang, J., Zheng, K.J., Zhu, Y., and Chen, H.M. (2020). Dynamic reoxidation/reduction-driven atomic interdiffusion for highly selective CO_2 reduction toward methane. J. Am. Chem. Soc. *142*, 12119–12132.

32. Firet, N.J., and Smith, W.A. (2017). Probing the reaction mechanism of CO_2 electroreduction over Ag films via operando

infrared spectroscopy. ACS Catal *7*, 606–612.

33. Pérez-Gallent, E., Figueiredo, M.C., Calle-Vallejo, F., and Koper, M.T. (2017). Spectroscopic observation of a hydrogenated CO dimer intermediate during CO reduction on Cu(100) electrodes. Angew. Chem. Int. Ed. Engl. *56*, 3621–3624.

34. Wuttig, A., Liu, C., Peng, Q., Yaguchi, M., Hendon, C.H., Motobayashi, K., Ye, S., Osawa, M., and Surendranath, Y. (2016). Tracking a common surface-bound intermediate during CO_2-to-fuels catalysis. ACS Cent. Sci. *2*, 522–528.

35. Zhu, S., Jiang, B., Cai, W.B., and Shao, M. (2017). Direct observation on reaction intermediates and the role of bicarbonate anions in CO_2 electrochemical reduction reaction on Cu surfaces. J. Am. Chem. Soc. *139*, 15664–15667.

36. Li, F., Li, Y.C., Wang, Z., Li, J., Nam, D.H., Lum, Y., Luo, M., Wang, X., Ozden, A., Hung, S.F., et al. (2020). Cooperative CO_2-to-ethanol conversion via enriched intermediates at molecule–metal catalyst interfaces. Nat. Catal. *3*, 75–82.

37. Kim, D., Resasco, J., Yu, Y., Asiri, A.M., and Yang, P. (2014). Synergistic geometric and electronic effects for electrochemical reduction of carbon dioxide using gold-copper bimetallic nanoparticles. Nat. Commun. *5*, 4948.

38. Zheng, Y., Vasileff, A., Zhou, X., Jiao, Y., Jaroniec, M., and Qiao, S.Z. (2019). Understanding the roadmap for electrochemical reduction of CO_2 to multi-carbon oxygenates and hydrocarbons on copper-based catalysts. J. Am. Chem. Soc. *141*, 7646–7659.

39. Wang, Y., Wang, Z., Dinh, C.T., Li, J., Ozden, A., Golam Kibria, M.G., Seifitokaldani, A., Tan, C.S., Gabardo, C.M., Luo, M., et al. (2020). Catalyst synthesis under CO_2 electroreduction favors faceting and promotes renewable fuels electrosynthesis. Nat. Catal. *3*, 98–106.